Micro-mechanism of multi-pathway activation peroxymonosulfate by copper-doped cobalt silicate: The dual role of copper

Lulu Long [a],[*],[1], Linlin Su [a],[1], Wei Hu [a], Shihuai Deng [a], Chao Chen [a], Fei Shen [a], Min Xu [a], Guixiang Huang [b], Gang Yang [a],[*]

[a] *Institute of Ecological and Environmental Sciences, Sichuan Agricultural University, Sichuan 611130, China*
[b] *CAS Key Laboratory of Urban Pollutant Conversion, Department of Chemistry, University of Science & Technology of China, Hefei 230026, China*

ARTICLE INFO

ABSTRACT

Bimetallic catalysts tend to show excellent catalytic performance to activate peroxymonosulfate (PMS) due to the synergistic effect. Although the outstanding catalytic ability of metal silicates to activate PMS has been clarified for a long time, the synergistic effect and micro-mechanism of bimetal in silicate are still being ignored. In this work, we prepared Cu-doped cobalt silicate (CuCoSi) hollow nanospheres to confirm the synergistic effect of bimetal in silicate for activating PMS. A novel and comprehensive synergistic micro-mechanism at the molecular and electronic levels is proposed. Experimental and theoretical analysis reveals that Co provides unique active sites in CuCoSi and Cu enhances the radical pathway by electron transfer with Co instead of directly participating in the activation of PMS. The increased oxygen vacancies (Ov) in the material promotes the formation of $^1O_2$ due to Cu doping. This work lays a foundation of the development of bimetallic silicates catalysts.

1. Introduction

To efficiently remove refractory organic pollutants from water, sulfate radical-based advanced oxidation processes (SR-AOPs) have been developed [1–5]. Compared with Fenton (or Fenton-like) techniques, SR-AOPs are provided with stronger redox ability, a wider pH range, and a longer half-period [6–11]. Among the many ways to activate peroxymonosulfate (PMS), transition metal activation is considered to be one of the most promising due to its simple operation and there being no need to input additional energy [12]. Generally, Co, Mn, Fe, and Cu are the transition metals commonly used to activate PMS. Among them, Co is considered to be the most effective transition metal for activating PMS [13]. CoO_x, $CoMO_x$ (M = Cu, Fe, or Mn), and some supported cobalt-based catalysts, such as Co@N-C and Fe_3O_4@Zn/Co-ZIFs, are common cobalt-based catalysts [14–17]. Among these cobalt oxide catalysts, bimetallic catalysts tend to show better catalytic activity and stability compared with single metal catalysts, which is mainly attributed to the interaction between the two metals [18–21]. For example, the synergistic effect of Cu, Fe, and Co gives a $CuFe_2O_4$-$CoFe_2O_4$ composite catalyst with excellent catalytic activity and stability [22].

In addition to oxides, metal silicates are also widely used for

pollutant degradation due to their high hydrophilicity and large specific surface area [23]. The catalytic activity of metal silicates, such as cobalt silicate (CoSi), copper silicate (CuSi), nickel silicate, iron silicate, and magnesium silicate for PMS was investigated. Due to the high reactivity of Co for PMS, CoSi showed the best catalytic activity among these silicates [24]. At present, although the catalytic ability of CoSi to activate PMS has been clarified, methods to further improve the activity and practical application potential of a CoSi/PMS system have still attracted a lot of attention. Some researchers have prepared CoSi with a special structure, such as hollow spheres, which makes the active sites of the material more dispersed and improves the utilization rate of the catalyst [23,24].

Moreover, considering the synergistic effect of bimetals in oxides, metal doping may be one of the effective ways to optimize the catalytic performance of CoSi [14,18,19,22]. As we known, most of metal silicates have obvious distinction with oxides such as more disordered crystal structure and more defects (oxygen vacancies (Ov), et al.) [23], which may make the synergistic effect of the bimetal in the silicate more diversified than in the oxide. Hence, it is necessary to confirm whether the doped foreign metal in silicate has the same synergistic effect as it does in the oxide. Notably some researchers have recently pointed out

that the active site may be unique to one of the metals [14,18], which is different from traditional mechanism of two metals are both active sites in bimetallic oxide. Although the unique-site mechanism in bimetal oxides has been reported, the similar mechanism usually happened on a bimetallic system with the inability of foreign metals to activate PMS. Therefore, for a deeper understanding of the synergistic mechanism, it is also essential to clarify the active sites in the bimetallic silicate/PMS system. Moreover, the synergistic effect of bimetals in oxides is usually reflected only in the radical pathway, whereas relevant studies have shown that the Ov of cobalt silicate itself will bring a large amount of singlet oxygen ($^1O_2$) besides the free radical pathway [23,24]. Above of all, for better improving the activity of metal silicates, a comprehensive and further study on synergistic effect and mechanism of bimetallic silicates including radical and non-radical pathway should not be neglected.

In this work, to respond to the above issues, we prepared Cu-doped cobalt silicate (CuCoSi) hollow nanospheres by an alcohol-thermal method using SiO_2 as a template. Compared with CoSi, CuCoSi had better catalytic activity and stability for activating PMS, which indicated that there was a synergistic effect between Co and Cu in silicate. The experimental results from electron paramagnetic resonance (EPR) and X-ray photoelectron spectroscopy (XPS) showed that Cu doping not only promoted the radical pathway but it also promoted the non-radical pathways. Notably, from the point of view of a microscopic mechanism, it was proved that Co was the unique active site for catalyzing PMS. Cu doping enhanced the radical pathway by electron transfer with Co instead of directly participating in the activation of PMS, although CuSi could effectively activate PMS. Furthermore, it was found that non-radical pathways had been enhanced by the formation of more Ov due to Cu doping. Our findings reveal the bimetallic synergistic effect and mechanism in silicate and implied that the conventional perceptions on dual active sites of bimetallic catalysts might need re-evaluation.

2. Experimental procedures

2.1. Chemicals

Cobalt chloride ($CoCl_2.6H_2O$), anhydrous ethanol (EtOH), sodium chloride (NaCl), sodium nitrate ($NaNO_3$), sodium bicarbonate ($NaHCO_3$), and sodium dihydrogen phosphate (NaH_2PO_3) were provided by Chengdu Kelong Chemical Co., Ltd. Ammonia water ($NH_3.2H_2O$) and methanol (MeOH) were provided by Xilong Chemical Co., Ltd. Tetraethyl orthosilicate (TEOS), tetracycline (TC), potassium peroxymonosulfate (PMS), 5,5-dimethyl-1-pyrroline N-oxide (DMPO), and 2,2,6,6-Tetramethyl-4-Piperidone (TEMP) were provided by Aladdin Bio-Chem Technol. Copper (II) chloride dihydrate ($CuCl_2.2H_2O$), tert-Butanol (TBA), and L-Histidine were provided by Sinopharm Chemical Reagents Co. Ltd.

2.2. Catalyst preparation

SiO_2 nanospheres and CuSi hollow nanospheres were synthesized by improved Stöber method and hydrothermal method, respectively. See the Supporting Information for detailed preparation steps. CoSi was synthesized by an alcohol-thermal method. First, 0.8 mL deionized water (DI), 4 mL 28% $NH_3 \cdot H_2O$, and 1.8 mmol $CoCl_2.6H_2O$ were added into a 25 mL beaker for ultrasound. Then 0.14 g SiO_2 was added to the above beaker with magnetic stirring for 30 min, followed by the addition of 8 mL of EtOH with continuous stirring. The obtained mixed solution was transferred to a 25 mL Teflon autoclave and maintained at 180 ℃ for 24 h. Finally, the final product was separated by centrifugation, washed several times with DI and EtOH, and dried at 60 ℃ for 12 h to obtain CoSi. The synthesis of CuCoSi was similar to CoSi. Cu_1Co_5Si, Cu_1Co_1Si, $Cu_{1.5}Co_1Si$, and Cu_2Co_1Si were obtained by maintaining the total molar amount of $CoCl_2.6H_2O$ and $CuCl_2.2H_2O$ at 1.8 mmol and changing the molar ratios of $CoCl_2.6H_2O$ and $CuCl_2.2H_2O$ at 5:1, 1:1,

1:1.5 and 1:2, respectively. CuCoSi represented $Cu_{1.5}Co_1Si$.

2.3. Catalyst characterization

The morphology and structure of CuCoSi were characterized by scanning electron microscopy (SEM, Zeiss Sigma 300, Germany), transmission electron microscopy (TEM, FEI Tecnai F20, USA), high-resolution transmission electron microscopy (HRTEM, FEI Tecnai F20, USA), X-ray diffraction (XRD, X′Pert PRO MPD, Netherlands), and Fourier Transform Infrared Spectrometer (FTIR, Nicolet iS 10, USA). The Brunauer-Emmett-Teller (BET) and Barrett-Joyner-Halenda (BJH) methods were used to analyze specific surface area, pore volume and size (ASAP2020, USA). The concentration of metal ions was measured by inductively coupled plasma (ICP-MS: PerkinElmer NexION 300X, USA). The concentration of TC was measured at 360 nm using an ultraviolet-visible spectrophotometer (UV-2800A, USA). Electron paramagnetic resonance (EPR, Bruker EMXplus, Switzerland) was used to determine the free radical using DMPO/TEMP as the spin-trapping agent in the system and the oxygen vacancies of the materials. The chemical state of elements was determined by X-ray photoelectron spectroscopy (XPS, Thermo Kalpha, UK). The redox behavior was evaluated by hydrogen temperature programmed reduction (H_2-TPR) experiments on a chemisorption analyzer (AutoChem1 II 2920, Micromeritics Ltd., USA), seeing SI for details. The fluorescence probe experiment of $^1O_2$ was observed by laser confocal microscope (CLSM, Zeiss LSM 880, GER). The electrochemical workstation (CHI 600, China) was used to determine cyclic voltammetry curve of materials. The ultraviolet-visible (UV-Vi) absorption spectrum of the catalyst was measured by a diffuse reflectance spectrophotometry (Shimadzu UV3600, Japan). Finally, the degradation intermediate products were explored by liquid chromatography-mass spectrometry (LC-MS, Ultimate 3000 UHPLC-Q Exactive, USA).

2.4. Catalytic degradation experiments

TC was selected as the model pollutant to evaluate the catalytic performance of CuCoSi/PMS systems. A certain amount of CuCoSi was added into 80 mL TC solution (40 ppm) with ultraphonic for 5 min. The mixture was stirred for 20 min to reach adsorption equilibrium. Then, a certain amount of PMS was added to the solution. The concentration of TC was measured by UV-Vi spectrophotometer (λ = 360 nm) every 10 min after filtration. Degradation efficiency was evaluated by C_t/C_0. The degradation process conforms to the pseudo-first-order kinetics: ln (C_t/C_0) = -kt, wherein, C_0, C_t, k and t are the initial concentration of TC, the concentration of TC at time t, the rate constant, and the reaction time, respectively. To carry out the stability experiment, the used catalyst was separated by filtration. Then it was washed several times with deionized water and dried at 60 °C for subsequent cyclic degradation experiments. The initial pH was adjusted with HNO_3 and NaOH solution (1 M). The quenching experiment was used to preliminarily identify the active species of the CuCoSi/PMS/TC system using methanol (MeOH), tert-butanol (TBA), and L-histidine as masking agents. The Zeta potential of the catalyst suspension and TC solution under different pH conditions were measured.

2.5. Computational method

We have employed the Vienna Ab Initio Package (VASP) [25,26] to perform all the spin-polarized density functional theory (DFT) calculations within the generalized gradient approximation (GGA) using the PBE [27] formulation. We have chosen the projected augmented wave (PAW) potentials [28,29] to describe the ionic cores and take valence electrons into account using a plane wave basis set with a kinetic energy cutoff of 400 eV. Partial occupancies of the Kohn-Sham orbitals were allowed using the Gaussian smearing method and a width of 0.05 eV. The electronic energy was considered self-consistent when the energy
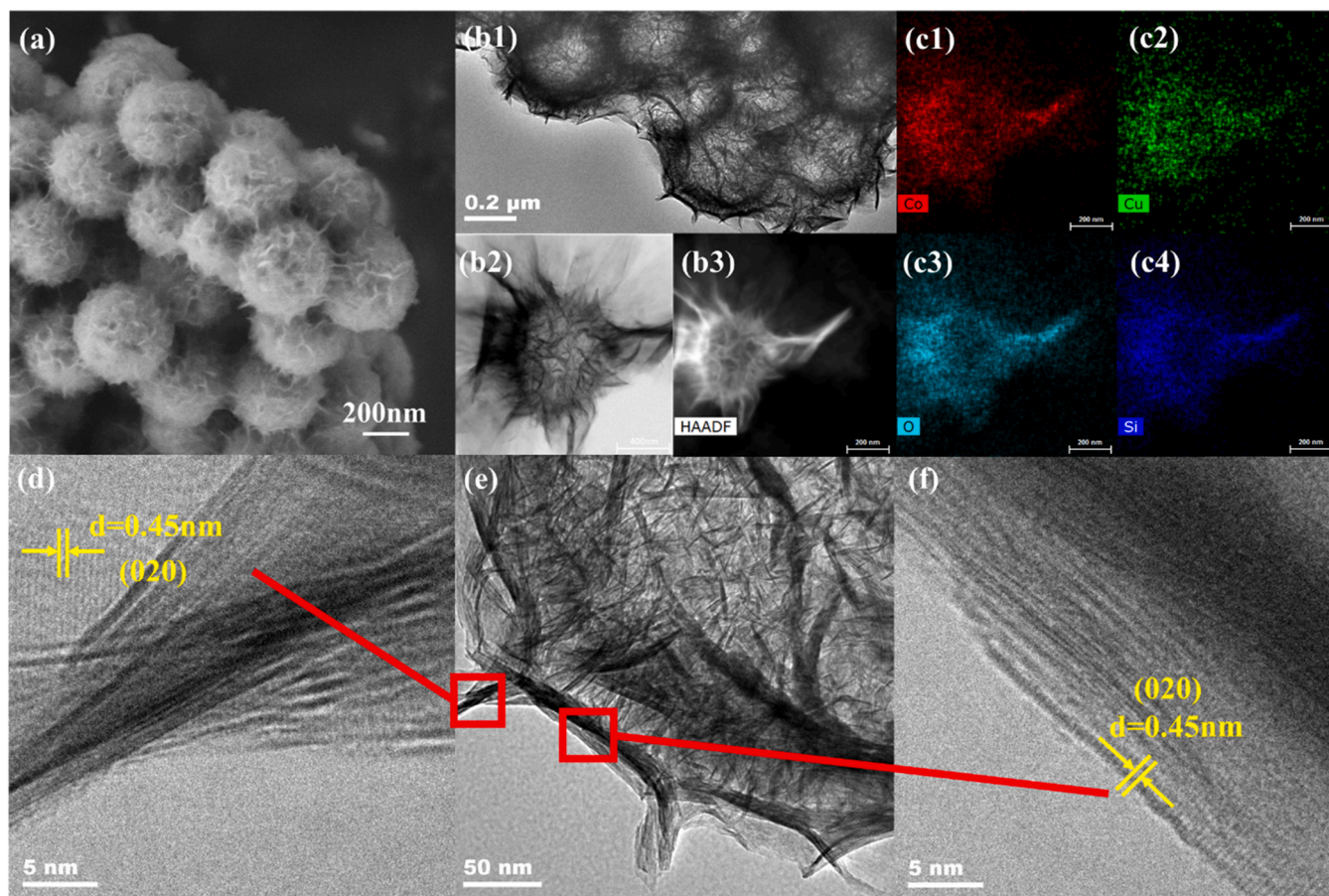
Fig. 1. (a) SEM image of CuCoSi; (b) TEM image of CuCoSi; (c) The corresponding EDS elemental mapping of Co, Mn, Si, and O; (d), (e), (f) HR-TEM images of CuCoSi.

change was smaller than 10^{-5} eV. A geometry optimization was considered convergent when the force change was smaller than 0.02 eV/Å. Grimme's DFT-D3 methodology [30] was used to describe the dispersion interactions.

The equilibrium lattice constants of orthorhombic Co_2SiO_4 unit cell were optimized, when using a $7 \times 5 \times 3$ Monkhorst-Pack k-point grid for Brillouin zone sampling, to be a = 4.607 Å, b = 5.797 Å, c = 9.816 Å. We then use it to construct a $Co_2SiO_4(010)$ surface model with p (2×2) periodicity in the x and y directions and 1 stoichiometric layer in the z direction seprated by a vacuum layer in the depth of 15 Å in order to separate the surface slab from its periodic duplicates. This surface model contains 32 Co, 16 Si and 64 O atoms. In another model, one Cu atom was doped into this $Co_2SiO_4(001)$ surface by replacing one Co atom on the outmost layer. During structural optimizations, the gamma point in the Brillouin zone was used for k-point sampling, and the bottom half layer was fixed while the top half was allowed to relax.

The adsorption energy (Eads) of adsorbate A was defined as.

$$E_{ads} = E_{A/surf} - E_{surf} - E_{A(g)}$$

where $E_{A/surf}$, E_{surf} and $E_{A(g)}$ are the energy of adsorbate A adsorbed on the surface, the energy of clean surface, and the energy of isolated A molecule in a cubic periodic box with a side length of 20 Å and a $1 \times 1 \times 1$ Monkhorst-Pack k-point grid for Brillouin zone sampling, respectively.

3. Results and discussion

### 3.1. Synthesis and characterization of catalysts

For the synthesis mechanism of the material, see Text 1 of SI. Fig. 1a shows scanning electron microscope (SEM) images of CuCoSi. As we can see, the size of the CuCoSi hollow nanospheres was uniform, and the average size was 380–420 nm. Similar to CoSi, the surface of the CuCoSi hollow nanospheres was composed of nanosheets (Fig. S1a). While the CuSi hollow nanospheres had a sea-urchin-like structure and the surface was composed of nano-needles, which gave CuSi excellent adsorption performance (Figs. S1b and S3). The results showed that CuCoSi was dominated by the CoSi structure and Cu was used only as a doping element. In addition, the element distribution map also shows the successful doping with Cu (Fig. S2).

To further confirm the hollow structure of CuCoSi, transmission electron microscopy (TEM) analysis was carried out. As shown in Fig. 1b, the surface of the CuCoSi hollow spheres was formed by a large number of interlaced nanosheets. The TEM element distribution map shows the elemental composition and distribution of CuCoSi. The elements Co, Cu, O, and Si in the CuCoSi sample were evenly distributed, which also showed the successful doping with Cu (Fig. 1c). It was further analyzed by ICP that the ratio of Co/Cu atoms in CuCoSi was 9:1. Fig. 1d, e, and f show HRTEM images of CuCoSi. The lattice fringe of 0.45 nm is similar to the (020) interplanar spacing in CoSi.

The successful preparation of SiO_2, CoSi, CuSi, and CuCoSi was verified with X-ray diffraction (XRD) spectra and Fourier transform infrared (FT-IR) spectroscopy. The wide peak shape and weak peak strength of SiO_2, CoSi, and CuSi revealed their low crystallinity (Fig. S4) [23]. Fig. 2a shows the XRD patterns of CuCoSi with different doping ratios. The diffraction peaks at $2\theta = 9.3$, 19.3, 35.3, and 60.4 were attributed to the peaks of $CoSiO_x$ (PDF#21–0871). The peak of $CuSiO_x$ (PDF#27–0188) was difficult to observe, which was attributed to a small amount of Cu doping.
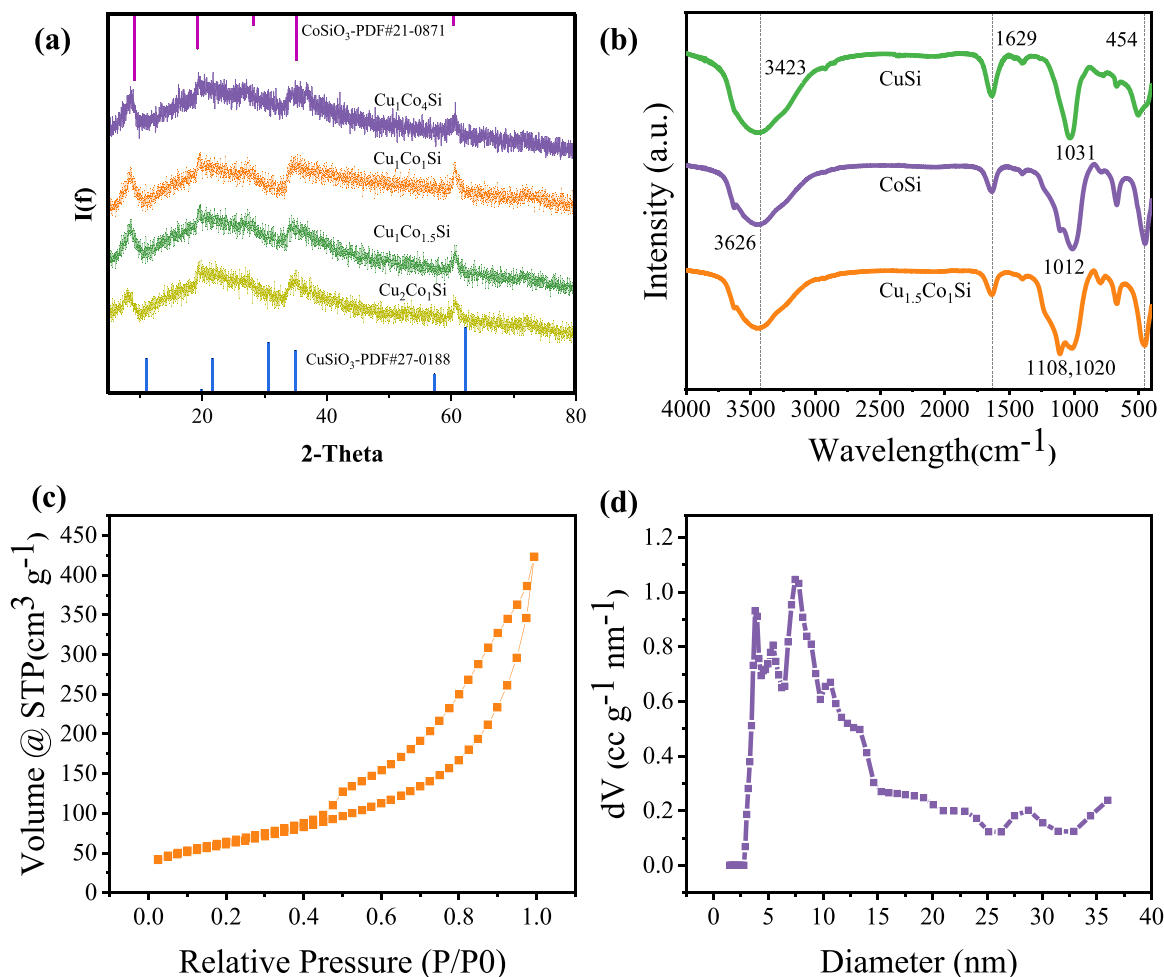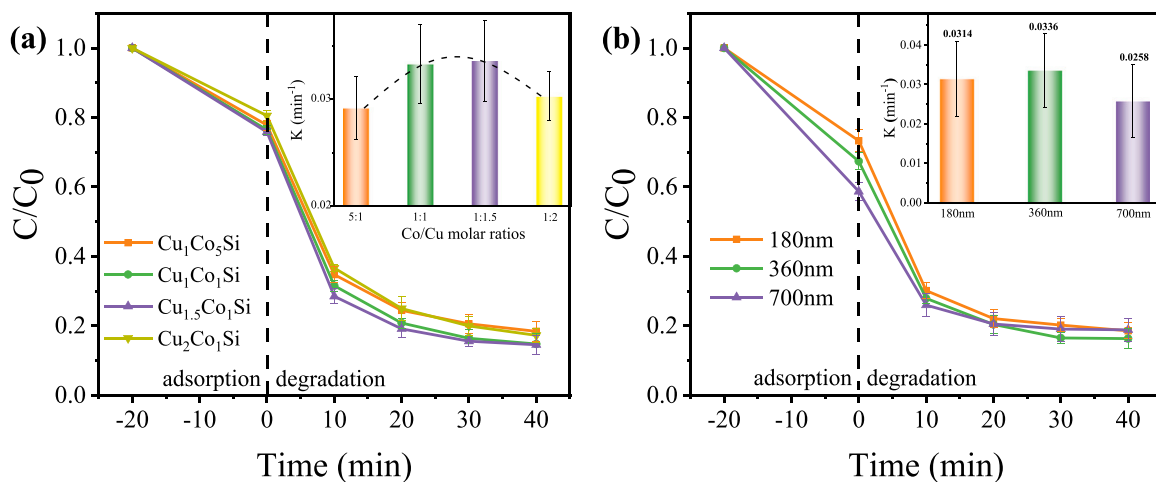
Fig. 2. (a) XRD of CuCoSi with different Cu doping ratios; (b) FT-IR of CoSi, CuSi, and CuCoSi; (c) N_2 adsorption-desorption isotherms; (d) DFT pore size distribution curves of CuCoSi.

Fig. 2b shows the FT-IR spectrum of the prepared metal silicate. The characteristic bands of 454 cm^{-1}, 1629 cm^{-1}, and 3423 cm^{-1} of metal silicate were attributed to the Si-O bond, the hydroxyl group of physically adsorbed water molecules, and the hydroxyl group bonded by hydrogen bonds, respectively [23]. The peak of CuSi at 1031 cm^{-1} was attributed to the vibration of the Cu-O-Si bond [31,32]. The peak of CoSi at 1012 cm^{-1} was attributed to the vibration of the Co-O-Si bond [23]. However, the FT-IR spectra of CuCoSi showed peaks at 1020 cm^{-1} and

Fig. 3. (a)Influence of CuCoSi with different Cu doping ratio on TC removal efficiency; inset: degradation rate constant, [reaction conditions: PMS concentration = 0.1 g L^{-1}, TC concentration = 40 ppm, CuCoSi concentration = 0.0625 g L^{-1}, reaction temperature = 25 °C and initial pH value = 7]; (b) Influence of CuCoSi synthesized different sizes SiO$_2$ on TC removal efficiency; inset: degradation rate constant, [reaction conditions: PMS concentration = 0.1 g L^{-1}, TC concentration = 40 ppm, CuCoSi concentration = 0.0625 g L^{-1}, reaction temperature = 25 °C and initial pH value = 7].
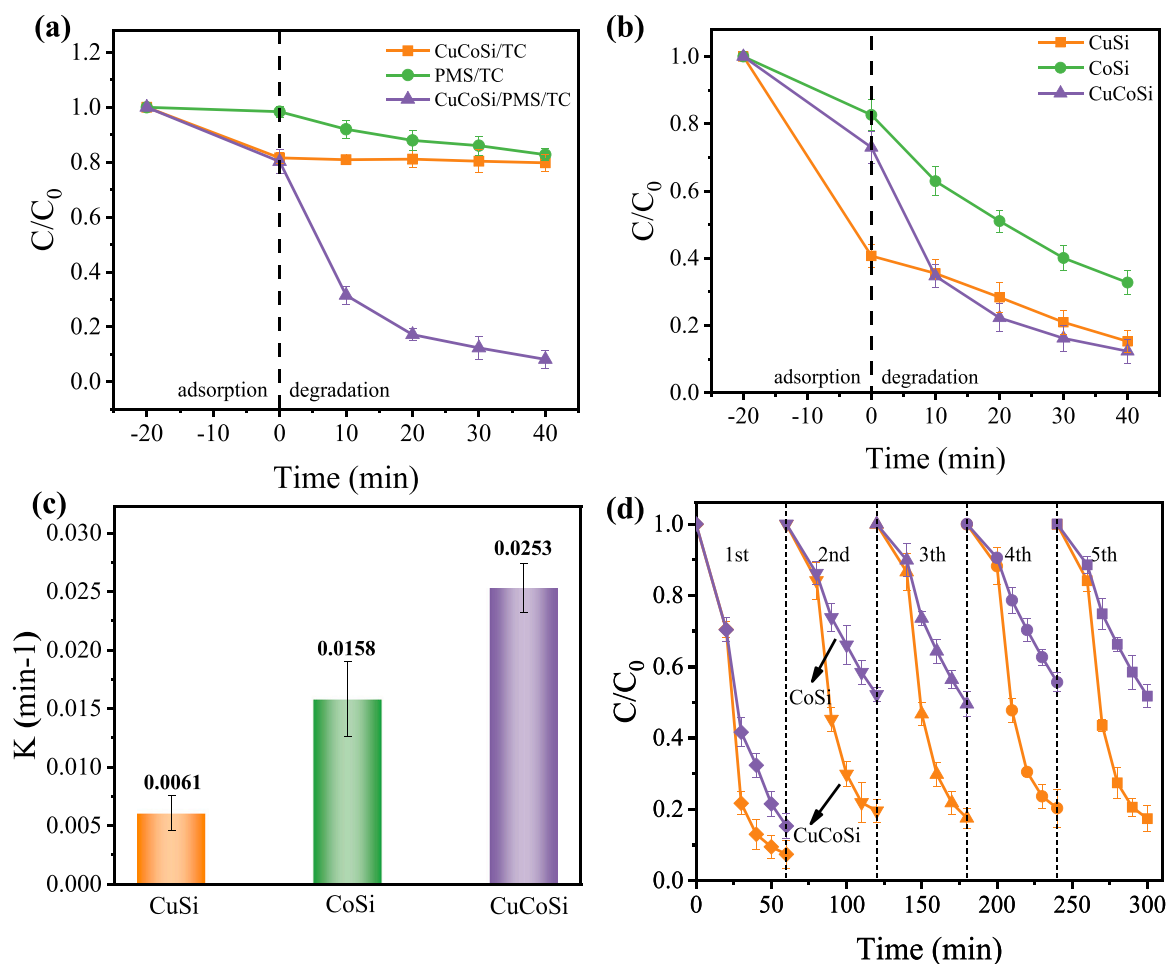
Fig. 4. (a) The removal efficiency and (b) degradation rate constant of CoSi, CuSi and CuCoSi for TC; [reaction conditions: PMS concentration = 0.15 g L^{-1}, TC concentration = 40 ppm, CuCoSi concentration = 0.0625 g L^{-1}, reaction temperature = 25 ℃ and initial pH value = 7]; (c) Reusability of CuCoSi and CoSi detection [reaction conditions: PMS concentration = 0.2 g L^{-1}, TC concentration = 40 ppm, reaction temperature = 25 ℃, CuCoSi Concentration = 0.1 g L^{-1} and initial pH value = 7]; (d) XPS spectra of fresh and used CuCoSi.

1108 cm^{-1}, indicating the vibration of the Co-O-Si bond and Cu-O-Si bond, respectively. The migration of the Co-O-Si and Cu-O-Si bonds was due to the doping with Cu. In addition, the peak at 3626 cm^{-1} was characteristic of CoSi and was attributed to the cobalt hydroxyl group [23].

The specific surface area and pore size distribution of CuCoSi will affect its catalytic performance and they were determined by N$_2$ adsorption-desorption. As shown in Fig. 2c, the N$_2$ adsorption-desorption isotherm of CuCoSi exhibited a typical type H1 of IV isotherm curve that is a characteristic feature of a uniform mesoporous structure [33,34]. Its specific surface area was 221.952 m^2 g^{-1}. The aperture distribution was calculated by the density functional theory (DFT) method. As shown in Fig. 2d, the pore sizes were mainly distributed between 3 and 15 nm. The average pore diameter is 11.82 nm.

3.2. Catalytic activity and stability evaluation

Tetracycline (TC) as a characteristic pollutant was used to evaluate the catalytic capacity of CuCoSi for PMS. Before the degradation, 10 min was required to reach adsorption equilibrium in CuCoSi/TC (Fig. S3). First of all, we examined the effect of the Co/Cu molar ratio on degradation performance (Fig. S5). With the increase in Cu doping amount, the degradation efficiency of TC continued to improve, and Cu$_{1.5}$Co$_1$Si showed the best degradation efficiency (Fig. 3a). Then, as the amount of Cu doping further increased, the degradation efficiency of CuCoSi began

to decrease. The reason might be that excessive Cu replaced a large amount of Co, which is considered to be the most effective transition metal for activating PMS. To further optimize the catalyst, we prepared SiO$_2$ spheres of different sizes to synthesize Cu$_{1.5}$Co$_1$Si (Fig. S6). As shown in Fig. 3b, CuCoSi synthesized from SiO$_2$ with a diameter of 360 nm has the very best degradation efficiency. Therefore, Cu$_{1.5}$Co$_1$Si synthesized from 360 nm SiO$_2$ spheres was selected for the subsequent degradation experiments.

Above all, the catalytic activity of CuCoSi was investigated. The ability of single PMS and catalyst to remove TC was extremely limited. However, added PMS in CuCoSi/TC system, TC was almost completely removed within 40 min (Fig. 4a). The degradation efficiency of TC was evaluated in different systems to confirm the synergistic effect of Co and Cu in silicate (Fig. 4b and c). The TC degradation rates of CuSi, CoSi, and CuCoSi were 0.0061, 0.0158 and 0.0253 min^{-1}, respectively, which indicated that Cu doping improved the degradation efficiency of CoSi. The stability of the CuCoSi/PMS system was evaluated by cyclic experiments (Fig. 4d). In the first cycle, the TC removal efficiency reached 95%. After the fifth cycles, the TC removal efficiency was stable at 80%. The possible reasons for the slight decrease might be the leaching of small amount of cobalt ion and the loss of active sites due to the adsorption of organic substances on the surface of the material [12,22, 35]. For comparison, after the second cycle of CoSi, the removal efficiency of TC rapidly decreased to 50%, indicating that the doping with Cu was conducive to improving the stability of CoSi (Fig. 4d). This might be attributed to the valence conversion and interaction between the Cu
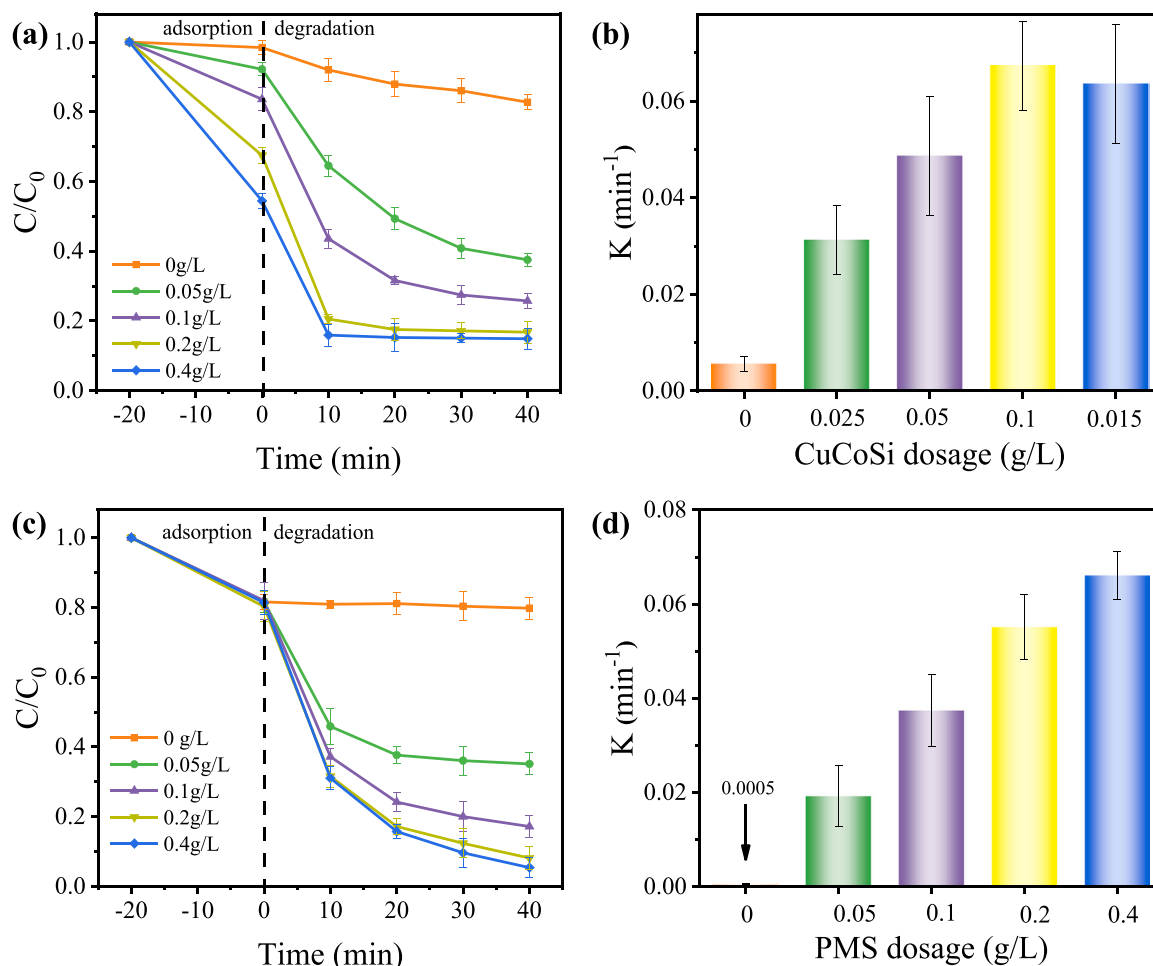
Fig. 5. Influence of CuCoSi dosage on TC removal efficiency: (a) removal efficiency and (b) degradation rate constant, [reaction conditions: PMS concentration = 0.1 g L^{-1}, TC concentration = 40 ppm, reaction temperature = 25 ℃ and initial pH value = 7]; Influence of PMS dosage on TC removal efficiency: (c) removal efficiency and (d) degradation rate constant, [reaction conditions: TC concentration = 40 ppm, CuCoSi concentration = 0.05 g L^{-1}, reaction temperature = 25 ℃ and initial pH value = 7].

and Co bimetals [20,21]. The stability of CuCoSi was further demonstrated by XPS spectra and the XRD spectra. As shown in Fig. S7a and S7b, the phase structure of the catalyst did not change significantly before and after the reaction. Moreover, the SEM images also indicated that both the fresh and used material surfaces maintained the nanosheet-like structure of CoSi, which demonstrated the stability of the catalyst structure. However, after the reaction, some of the gaps between the nanosheets were filled due to the residue of TC and its intermediates (Fig. S7c and S7d). Meanwhile , the leaching of metal ions was measured by ICP. Fig. S8 showed that the ion concentration of Co ions and Cu ions in the CuCoSi/PMS system were 0.8544 mg L^{-1} and 0.0368 mg L^{-1}, respectively, lower than the emission standard of industrial wastewater based on GB/T 25467–2010 of China(1.0 mg L^{-1} and 0.5 mg L^{-1}) [36]. The leaching ratio of Cu and Co ions were 1.57% and 4.25%, respectively. In summary, CuCoSi showed excellent catalytic activity and stability.

3.3. Evaluation of practical application potential

Optimization of the amount of catalyst will reduce the cost of pollutant treatment, so it is crucial to determine the effect of catalyst dosage on TC degradation. The degradation process of TC with different amounts of CuCoSi is shown in Fig. 5a. When only PMS was added, the degradation efficiency for TC was only 10%. When the amount of catalyst was 0–0.1 g L^{-1}, the degradation rate continued to increase

with the increase in the amount of catalyst. With a further increase in the amount of catalyst, the degradation rate began to decrease (Fig. 5b). This was because the excess catalyst became a scavenger of active oxygen, thereby limiting the reaction rate [37].

Similarly, the PMS dosage was evaluated to meet the needs of practical use (Fig. 5c and d). When the PMS dosage was 0 g L^{-1}, the removal of TC was attributed to the adsorption of CuCoSi. With the increase in PMS dosage from 0.05 g L^{-1} to 0.2 g L^{-1}, the degradation efficiency for TC increased significantly from 40% to 80%. Because excessive PMS competed with pollutants for SO$_4^-$·[37], the degradation efficiency for TC was not significantly improved with a continuous increase in the PMS dosage. Therefore, considering economy and efficiency, 0.2 g L^{-1} was considered the most suitable PMS dosage.

The effect of pH on the degradation of TC in the CuCoSi/PMS system was also evaluated (Fig. 6a). The zeta potentials of CuCoSi and TC were negative and became more negative as the pH value increased when the pH was in the range of 3–11(Fig. S9a). Therefore, CuCoSi had the lowest adsorption rate for TC at a pH value of 11. Under acidic conditions, the degradation efficiency of TC was low. However, under alkaline conditions, TC was unstable and would become an isomer with lactone structure to affect the degradation [38,39]. Therefore, a solution with pH = 7 was chosen for subsequent experiments. Moreover, to eliminate the influence of TC under alkaline conditions, we selected a typical dye Rhodamine B (RhB) as pollutants to conduct degradation experiments at different pH (Fig. S9b and S9c). The results showed that the degradation
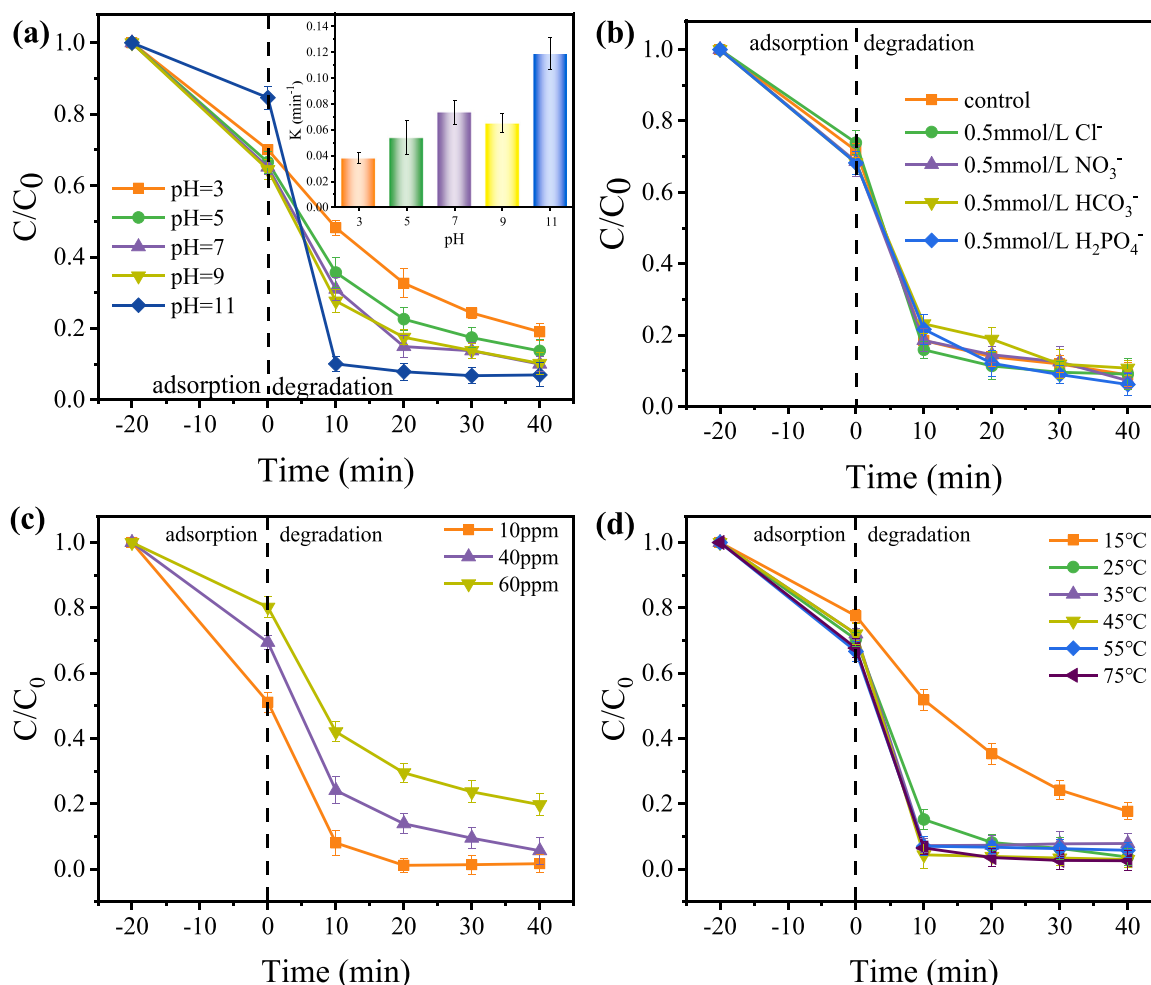
Fig. 6. (a) The influence of the initial pH on TC removal efficiency, inset: degradation rate constant, [reaction conditions: PMS concentration = 0.2 g L^{-1}, TC concentration = 40 ppm, reaction temperature = 25 °C and CuCoSi concentration = 0.1 g L^{-1}]; (b) The influence of inorganic anion on TC removal efficiency, [reaction conditions: PMS concentration = 0.2 g L^{-1}, TC concentration = 40 ppm, reaction temperature = 25 °C, CuCoSi concentration = 0.1 g L^{-1} and initial pH value = 7]; (c) The influence of the initial TC concentration on TC removal efficiency, inset: degradation rate constant, [reaction conditions: PMS concentration = 0.2 g L^{-1}, reaction temperature = 25 °C, CuCoSi concentration = 0.1 g L^{-1} and initial pH value = 7]; (d) The influence of reaction temperature on TC removal efficiency, [reaction conditions: PMS concentration = 0.2 g L^{-1}, TC concentration = 40 ppm, CuCoSi concentration = 0.1 g L^{-1} and initial pH value = 7].

of RhB was inhibited at pH = 3 and pH = 11. The above phenomenon might be attributed to: Under acidic conditions, $\cdot$OH and SO$_4^-\cdot$might react with H$^+$, reducing the degradation efficiency (Eqs.1–2) [23,37]. The CuCoSi zeta potential was negative and became more negative as the pH value increases when the pH was in the range of 3–11(Fig. S9a). Therefore, it was difficult for the catalyst to adsorb HSO$_5^-$ at pH = 11, resulting in a decrease in degradation efficiency. Moreover, under alkaline conditions, PMS might be consumed by OH$^-$ and decomposed S$_2$O$_5^{2-}$, resulting in a decrease in TC degradation [40].

$$\cdot OH + H^+ + e^- \rightarrow H_2O \tag{1}$$

$$SO_4^{\cdot-} + H^+ + e^- \rightarrow HSO_4^{\cdot-} \tag{2}$$

Common anions, such as Cl$^-$, NO$_3^-$, HCO$_3^-$, and H$_2$PO$_4^-$, may affect the degradation process by quenching the active species and occupying adsorption sites. 0.5 mmol/L Cl$^-$, NO$_3^-$, HCO$_3^-$, and H$_2$PO$_4^-$ were added to the reaction solution before the reaction began. Compared with the control group, the addition of anions had no significant effect on the removal efficiency for TC (Fig. 6b). This showed that, within a certain range, the CuCoSi/PMS system can adapt to changes in wastewater quality.

Adaptation to pollutant concentration change is one of important factors for evaluating the performance of a catalyst. Therefore, the effect

of pollutant concentration on TC removal efficiency is discussed in this work, with 10 ppm, 40 ppm, and 60 ppm as representative concentrations. As shown in Fig. 6c, the removal efficiency for TC at concentrations of 10 ppm and 40 ppm could reach more than 90% or even 100%. When the concentration was raised to 60 ppm, the removal efficiency of TC by CuCoSi was also maintained at about 80%. This indicated that the CuCoSi/PMS system had excellent removal efficiency for different initial concentrations of TC. Moreover, we also evaluated the ability of CoCuSi/PMS system to remove different pollutants. TC, RhB and Bisphenol A respectively represented several typical organic pollutants in water bodies: antibiotics, dyes and environmental hormones. As shown in Fig. S9d, the CoCuSi/PMS system had excellent removal efficiency for different types of organic pollutants, which indicated that the CoCuSi/PMS system had good universality.

To investigate the effect of temperature on the degradation of TC by the CuCoSi/PMS system, the temperature was maintained at 15 °C, 25 °C, 35 °C, 45 °C, 55 °C and 75 °C. As shown in Fig. 6d, the degradation efficiency was suppressed to a certain extent at 15 °C, but the removal efficiency could still be maintained at about 80%. The removal efficiency for TC reached nearly 100% as the temperature increased from 25 °C to 75 °C. The results showed that the CuCoSi/PMS system could adapt to a change in reaction temperature when removing TC, which would be beneficial to the practical application of CuCoSi.
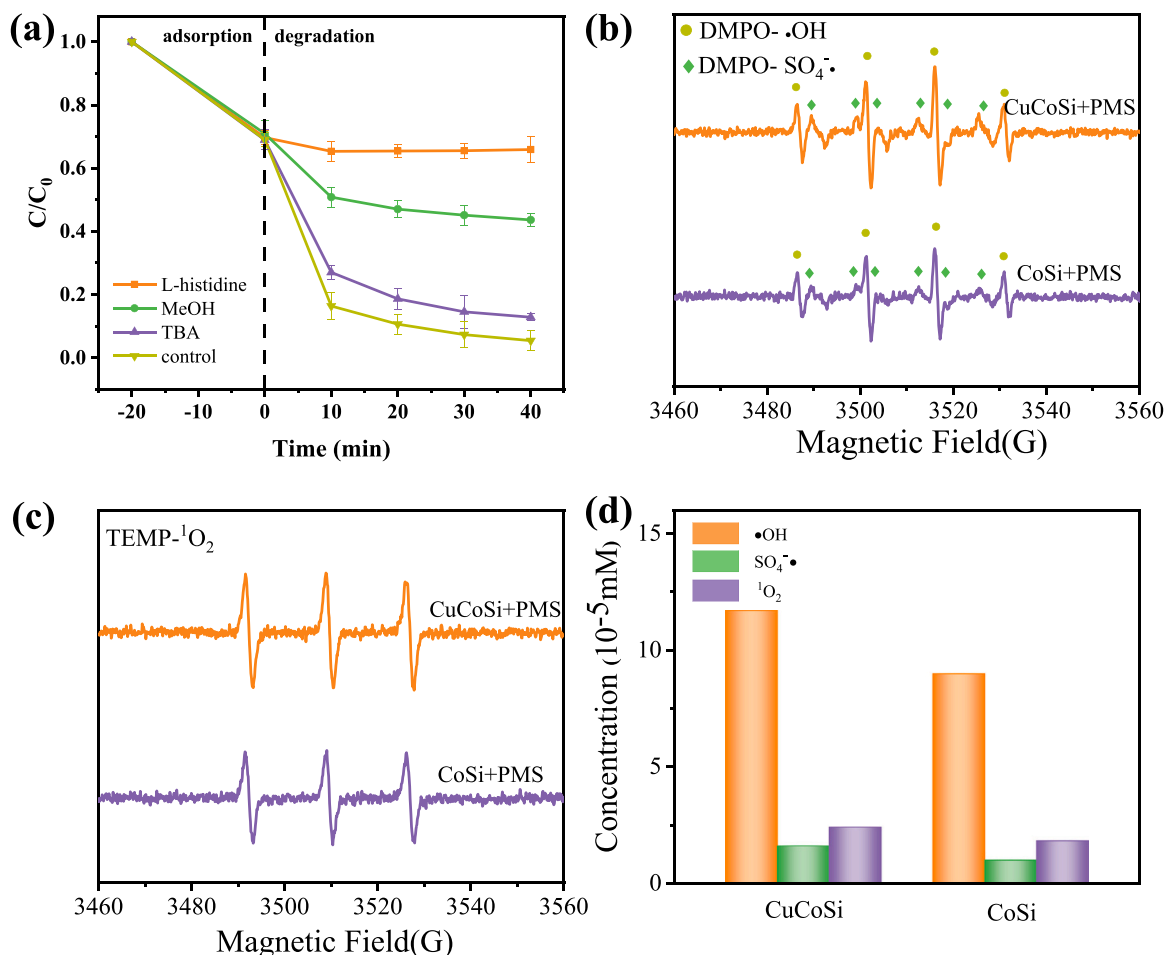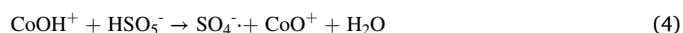
Fig. 7. (a) Effect of radical scavengers on TC removal efficiency; (b) EPR spectra of $SO_4^-\cdot$and$\cdot$OH in various reaction systems; (c) EPR spectra of $^1O_2$ in various reaction systems, [reaction conditions: PMS concentration = 0.2 g L^{-1}, TC concentration = 40 ppm, reaction temperature = 25 °C, CuCoSi concentration = 0.1 g L^{-1} and initial pH value = 7]; (d) Quantitative determination of $^1O_2$, $SO_4^-\cdot$and$\cdot$OH.
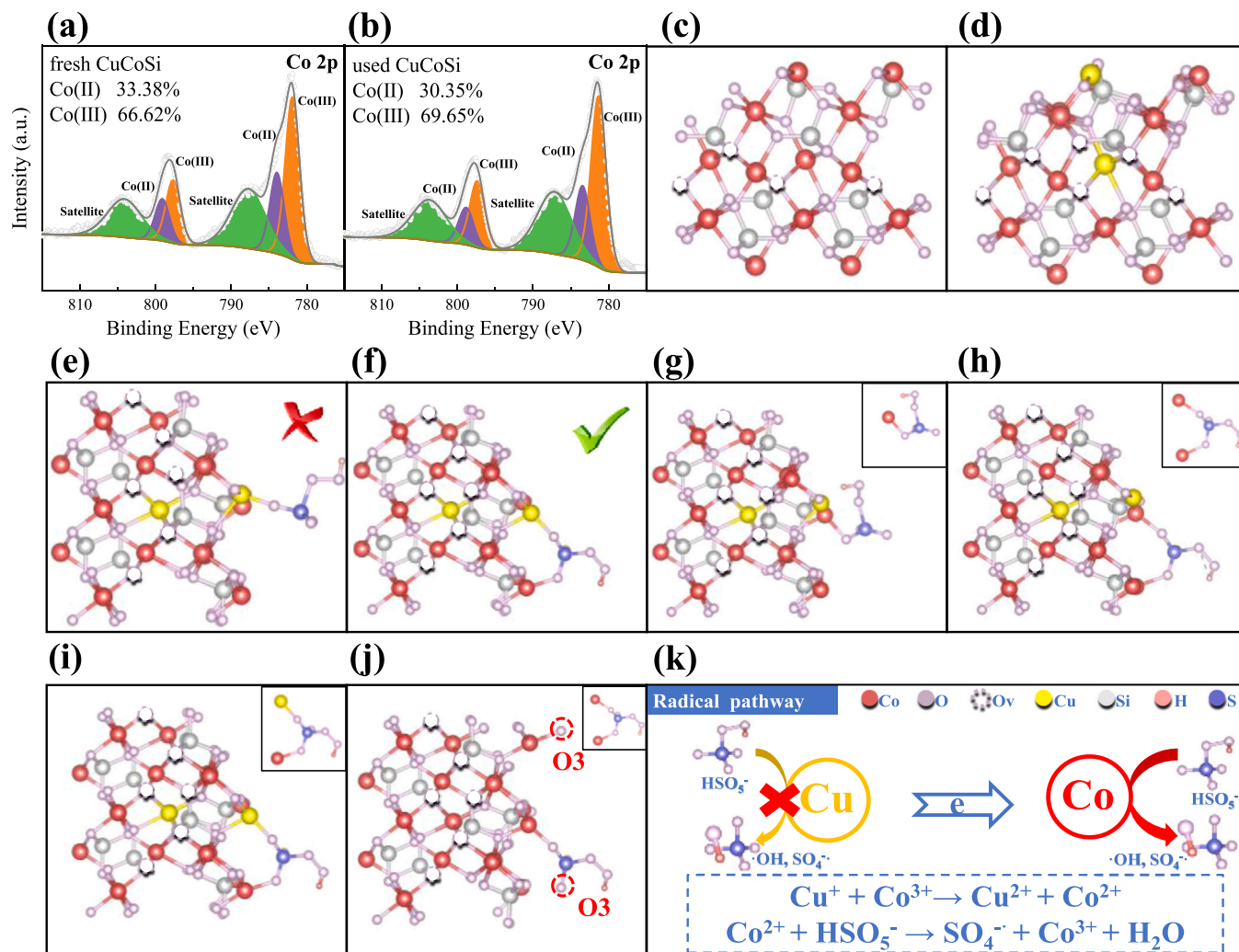
3.4. Identification of active species

According to reports, the possible active species were the sulfate radical ($SO_4^-\cdot$), hydroxyl radical ($\cdot$OH), and singlet oxygen ($^1O_2$) in the silicate/PMS/TC system [23,24]. Therefore, tert-butyl alcohol (TBA, a scavenger of $\cdot$OH), methanol (MeOH, a scavenger of $\cdot$OH and $SO_4^-\cdot$), and L-histidine (a scavenger of $^1O_2$) were used as masking agents for a masking experiment (Fig. 7a) [41]. Compared with the control group, the degradation efficiency for TC in the experimental group showed varying degrees of decline, indicating that the active species in the CuCoSi/PMS/TC system include $SO_4^-\cdot$ (Eqs. 3–6), $\cdot$OH (Eq. 7), and $^1O_2$ (Eqs. 8–10) [23]. However, recent studies have shown that the strong inhibitory effect of L-histidine on TC degradation was mainly due to the rapid consumption of PMS. Therefore, the influence of the presence of L-histidine on the concentration of PMS was explored. As depicted in Fig. S10a, the concentration of PMS in the CuCoSi/PMS/L-histidine system was similar to that in the CuCoSi/PMS system, which indicated that the consumption of PMS by L-histidine was limited. Therefore, the inhibition of degradation by L-histidine was mainly attributed to the reaction of L-histidine and $^1O_2$ instead of PMS, which was also consistent with the reaction rate constant of L-histidine and PMS, $^1O_2$ ($k_{\text{L-histidine, 1O2}}$ = 3.2 *10^7 M^{-1} s^{-1} >>$k_{\text{L-histidine, PMS}}$ = 10.9 M^{-1} s^{-1}) [42]. An experiment with nitrogen to eliminate oxygen also indicated that there was $^1O_2$ in the CuCoSi/PMS/TC system (Fig. S10b) [43]. Moreover, TC degradation experiments were carried out using acetone (to scavenger free radicals) as a solvent. Both the CuCoSi/PMS and CoSi/PMS systems could degrade TC to a certain extent, which also confirmed the existence
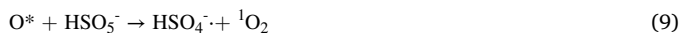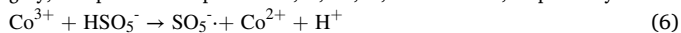
of $^1O_2$ (Fig. S10c) [44]. SOSG was used as a fluorescent probe of $^1O_2$ to confirm its existence of directly and accurately. The probe emitted green fluorescence (525 nm) after combined with $^1O_2$ [45]. As depicted in Fig. S11, green fluorescence was detected in CuCoSi/PMS system, which confirmed the presence of $^1O_2$. Notably, the green fluorescence mainly existed on the catalyst surface rather than in solution, which suggested that $^1O_2$ originated from the interfacial reaction of the catalyst and PMS rather than the self-decomposition of PMS. EPR experiments were further used to determine the active species of the CuCoSi/PMS and CoSi/PMS systems. As shown in Fig. 7b and c, when DMPO was added, the characteristic signal peaks of 1:2:1:2:1:2:1 was generated due to$\cdot$OH and $SO_4^-\cdot$[41]. Using TEMP as the spin-trapping agent, the characteristic signal of $^1O_2$ was detected: 1:1:1 [46]. Compared with the CuCoSi/PMS, the content of active species in the CuCoSi/PMS/TC system was decreased. The results indicated that the generated active species were used for the degradation of TC (Fig. S12). At the same time, the active species of the CoSi/PMS and CuCoSi/PMS systems were quantified through EPR [47]. Fig. 7d showed that Cu doping not only promoted the radical pathway, but also increased the generation of $^1O_2$, which was consistent with quenching experiments of CuCoSi/PMS and CoSi/PMS system (Fig. S10c and S13).

$$Co^{2+} + H_2O \rightarrow CoOH^+ + H^+ \tag{3}$$

$$CoOH^+ + HSO_5^- \rightarrow SO_4^-\cdot + CoO^+ + H_2O \tag{4}$$

$$CoO^+ + 2 H^+ \rightarrow Co^{3+} + H_2O \tag{5}$$

Fig. 8. High-resolution Co 2p XPS spectra of (a) fresh and (b) used CuCoSi; The atomistic structure of (c) CoSi and (d) CuCoSi; Optimized atomistic structure of PMS adsorption on the (e) Co sites of CuCoSi, (f) Co-Co sites of CuCoSi, (g) Co-Cu sites of CuCoSi, and (h) Co sites of CoSi; (i) Initial guess and (j) optimized atomistic structure of PMS adsorption on the Cu sites of CuCoSi; (k) Schematic diagram of the radical path mechanism of the CuCoSi/PMS system. The red, purple, yellow, gray, and pink balls represent Co, O, Cu, Si, and H atoms, respectively.

$$Co^{3+} + HSO_5^- \rightarrow SO_5^- \cdot + Co^{2+} + H^+ \qquad (6)$$

$$SO_4^- \cdot + H_2O/OH^- \rightarrow \cdot OH + SO_4^{2-} \qquad (7)$$

$$Ov \rightarrow O^* \qquad (8)$$

$$O^* + HSO_5^- \rightarrow HSO_4^- \cdot + {}^1O_2 \qquad (9)$$

3.5. The role of Cu in the radical pathway

To clarify the role of silicate doping with Cu, XPS was used to evaluate the changes in the chemical states of Co, Cu, and O in CoSi and CuCoSi before and after the reaction. As shown in Figs. 8a, b, S14a, and S14b, the characteristic peaks at 782.32 eV, 798.29 eV, 781.12 eV, and 797.03 eV were attributed to Co (II) and Co (III), respectively, and

Table 1
Adsorption energy of each model to PMS and PMS bard charge change.

Model	Adsorption energy (eV)	PMS Bard charge change (e)
CuCoSi-Co-PMS	-3.199	0.63
CuCoSi-Co-Co-PMS	-3.799	0.71
CuCoSi-Co-Cu-PMS	-4.176	0.68
CoSi-Co-CoPMS	-4.727	0.68

785.62 eV and 803.64 eV were allocated to the satellite peaks [13]. The content of Co (II) in CuCoSi and CoSi decreased by 3.03% and 6.88%, respectively, after used (Table S1). The lower decline of Co (II) in CuCoSi indicated that the doping of Cu promoted the reduction of Co(III) [18, 22,48]. H₂-temperature program reduction (H₂-TPR) further confirmed the above result. As shown in Fig. S15a, a reduction peak appeared at 387 °C in CoSi, which was considered to reduce Co(III) to Co(II) in H₂-TPR [11,18,49–51]. However, the reduction peak was found at a lower temperature (282 °C) in CuCoSi, indicating that the doped Cu might promote reduction of Co(III). In the cyclic voltammetry (CV) test (Fig S15b), when CoSi was selected as the working electrode, the redox current was slow. However, the redox current was significantly increased using CuCoSi as the working electrode, which indicated that the electron flow in CuCoSi was smoother [18,52]. Moreover, the UV-Vi absorption spectrum proved that the Cu doping reduced the energy band gap of CuCoSi (CuCoSi: 3.14 eV, CoSi: 3.17 eV), which indicated the lower barrier of electron transfer in CuCoSi (Fig. S15c) [52].

Moreover, to further clarify the synergistic effect of Co-Cu in silicate, DFT calculation was used to analyze the micro-mechanism. Clean CoSi and CuCoSi (010) models were constructed (Fig. 8c and d). The atomic ratio of Co and Cu in the CuCoSi models was 9:1, consistent with the result from ICP. In CuCoSi, PMS might be adsorbed with Co, Cu, Co-Co, and Co-Cu. Nevertheless, it is worth mentioning that it was difficult for
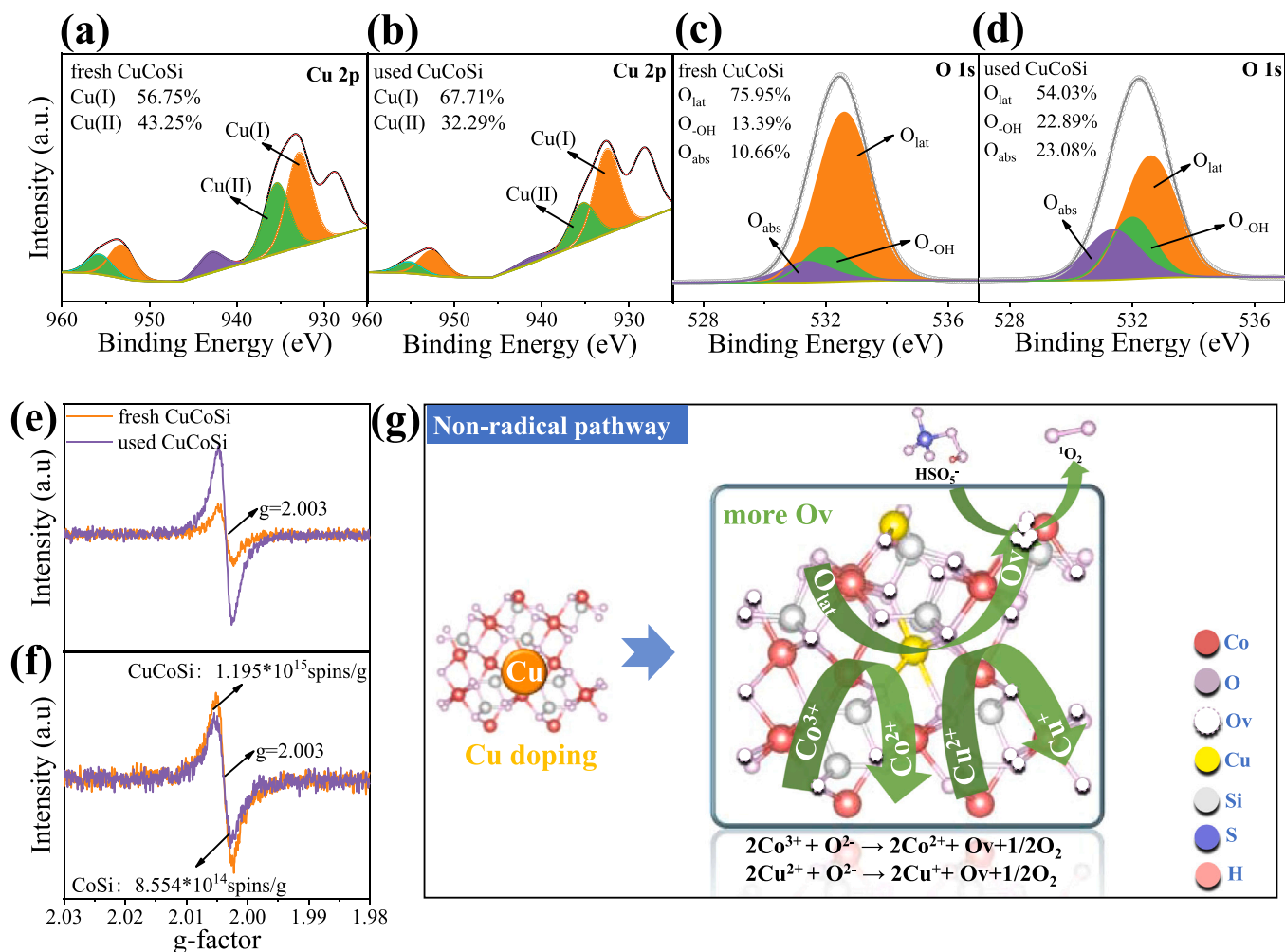
Fig. 9. High-resolution Cu 2p XPS spectra of (a) fresh and (b) used CuCoSi; High-resolution O 1s XPS spectra of (c) fresh and (d) used CuCoSi; (e) (f) The EPR spectra of fresh CuCoSi, used CuCoSi, and fresh CoSi (O_v); (g) Schematic diagram of the non-radical path mechanism of the CuCoSi/PMS system. The red, purple, yellow, gray, and pink balls represent Co, O, Cu, Si, and H atoms, respectively. The purple hollow balls represent O_v.

Cu to adsorb PMS stably and the model of Cu-PMS became bidentate adsorption of Co-Cu-PMS after optimization (Fig. 8e and f). The optimized structure of the remaining three models is shown in Fig. 8g-i. To better understand the activation of PMS by CuCoSi, the adsorption energy and Bard charges of the three models of Co-PMS, Co-Co-PMS, and Co-Cu-PMS were investigated. As shown in Table 1, the adsorption energies of PMS and Co, Co-Co, and Co-Cu were − 3.199 eV, − 3.799 eV, and − 4.176 eV, respectively. Because smaller and larger adsorption energies hindered the adsorption and dissociation of PMS on CuCoSi, neither of them was conducive to the activation of PMS [11,53]. This result indicated that Co-Co might be the prioritized active site for PMS activation. Further analysis of the changes in the Bard charge revealed that the charge transfer between PMS and CuCoSi was 0.63 e, 0.71 e, and 0.68 e, respectively (Table 1). There was the strongest charge transfer within Co-Co-PMS. At the same time, the low doping amount of Cu and the steric hindrance effect made it difficult for Co-Cu to activate PMS as active sites. Therefore, Co-Co in CuCoSi was considered to be the prioritized active site, and Cu did not directly participate in the activation of PMS. In addition, the adsorption model of Co-Co-PMS in CoSi (010) was established (Fig. 8j), and the adsorption energy and Bard charge are shown in Table 1. Compared with CoSi, CuCoSi had more suitable adsorption energy and stronger charge transfer, which indicated that the doping with Cu enhanced the activation of PMS by CoSi.

To clarify the contribution of Cu to the radical pathway, the Bard charge change of Cu was analyzed in detail. In the Co-Co-PMS model,

the total Bard change of Cu was − 0.07 e, which indicated that Cu lost electrons after PMS was adsorbed. Nevertheless, previous analysis showed that Cu was not the active site of PMS, so that it was difficult to directly transfer charge with PMS. Therefore, we speculated that Cu enhanced the activation of PMS by transferring electrons to Co, which was consistent with the above experimental results (Fig. S15, Eq. (10)) [18,22,48]. The O_{lat} could also reduce Co (III) except for Cu (I) in the process of activating PMS (Scheme S2) [13,23,54,55]. The Bard charge changes of O in CoSi and CuCoSi were also analyzed. It was found that the charge of O in CoSi and CuCoSi decreased by 2.04 eV and 1.94 eV, respectively. This indicated that the contributions of activated O_{lat} in CoSi and CuCoSi during the reduction of metal ions were comparable, and even more in CoSi. Therefore, based on the above results, compared with CoSi, more Co (III) in CuCoSi was reduced mainly from the oxidation of Cu (I) to Cu (II). Fig. 8k shows the reaction mechanism of the radical pathway of CuCoSi/PMS system.

$$Cu^+ + Co^{3+} \rightarrow Cu^{2+} + Co^{2+} \qquad (10)$$

3.6. The role of Cu in the non-radical pathway

Cu doping enhanced the non-radical pathway mainly by promoting the generation of O_v. As shown by the XPS spectra of Cu 2p (Fig. 9a and b), Cu(I) (932.87 eV, 953.19 eV), and Cu(II) (935.43 eV, 955.72 eV)
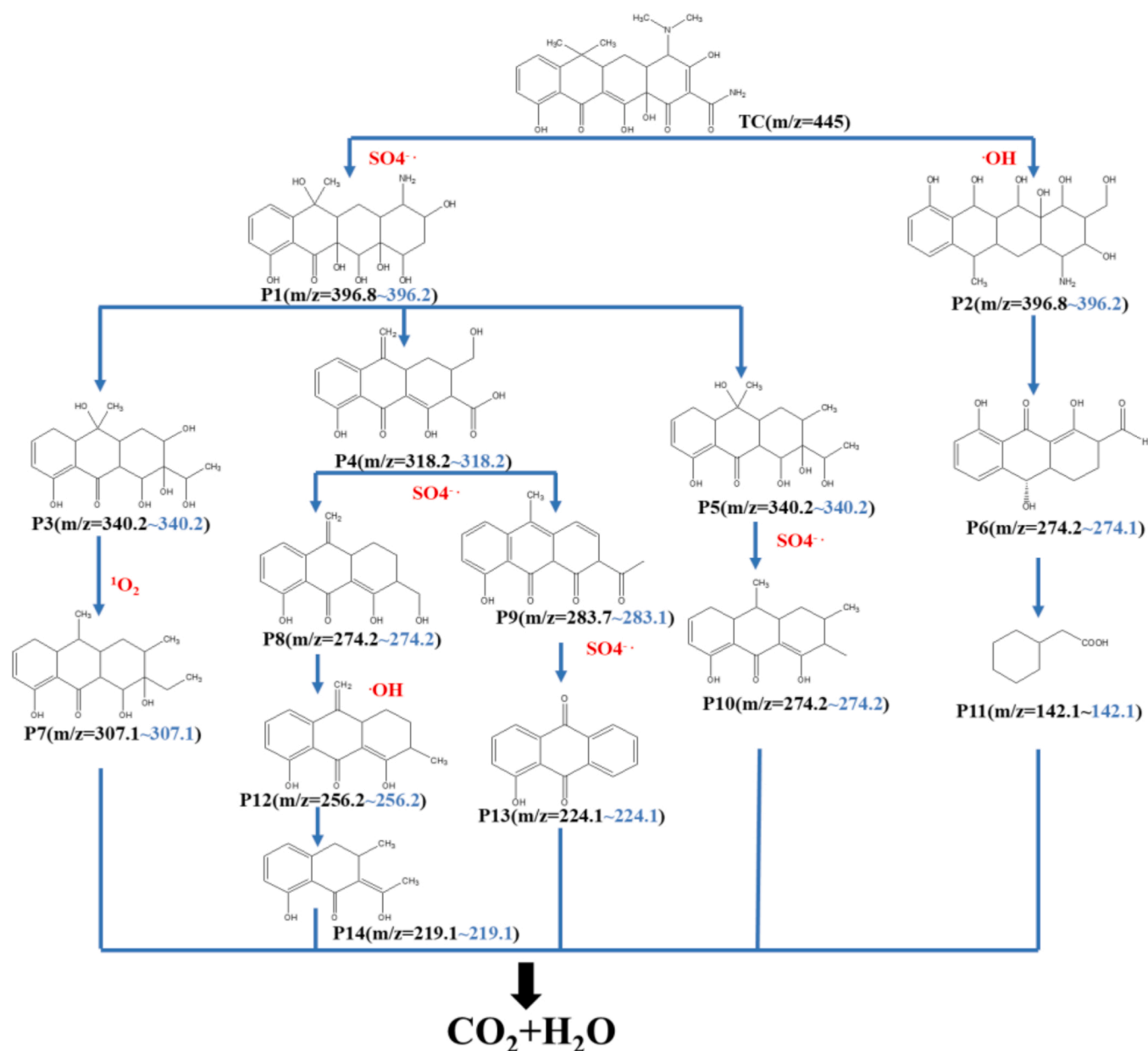
Fig. 10. The proposed decomposition pathways of TC in PMS/CuCoSi reaction system. The black values represent the measured values, and the blue values represent the theoretical values.

were detected, accompanied by a satellite peak at 942.94 eV [18]. The peak at 928.5 eV was attributed to Co 2s [56]. An increase in Cu (I) content in CuCoSi was also observed after the reaction, which was related to the formation of Ov (Scheme S2) [23]. Simultaneously, as observed from the O 1 s XPS spectrum, the fitted peaks at 533.15 eV, 532.55 eV, and 531.92 eV correspond to lattice oxygen (O_{lat}), hydroxyl oxygen (O_{-OH}), and adsorbed oxygen (O_{abs}), respectively (Fig. 9c and d). To a certain extent, the O_{abs} reflected the O_v content of the material [13]. Compared with fresh CuCoSi, the O_{lat} in the used CuCoSi was reduced, and the O_{abs} was increased. EPR was used to further verify the increase in O_v in CuCoSi after the reaction (Fig. 9e), which confirmed the $^1O_2$ generation pathway (Eqs. (8,9)) [15,23,57]. Moreover, fresh CuCoSi had more O_{abs} than fresh CoSi, indicating that fresh CuCoSi might have more Ov than fresh CoSi (Fig. S16). The result was further identified by EPR to quantify Ov (Fig. 8f). Moreover, the density of states (DOS) was added to further analyze the formation of Ov. As depicted in Fig. S17, the O p-band center relative to the Fermi level in CuCoSi was higher than in

CoSi, which was beneficial to the formation of Ov [14]. The above experimental results all indicate the important role of Cu in the formation of Ov. The reaction mechanism of the non-radical pathway is shown in Fig. 9g.

3.7. TC degradation pathway

To clarify the degradation process of TC, the intermediate products were detected by liquid chromatography-mass spectrometry (LC-MS). The results showed that there were 14 main intermediates (Fig. S18). Based on the results of LC-MS, possible degradation pathways for TC were proposed (Fig. 10). First, TC was attacked by $SO_4^{-\cdot}$ and·OH, and the alkyl and amino groups were dealkylated to form P1 and P2 ($m/z = 393$) [58], respectively. P1 and P2 were further attacked by the active species to form P3 ($m/z = 339$), P4 ($m/z = 318$), P5 ($m/z = 338$), and P6 ($m/z = 274$) by dehydration and ring opening [59,60]. P3 was dealkylated to P7 ($m/z = 309$) through the action of $^1O_2$ [59]. P4 and P5

were continuously attacked by SO_4^-·to generate P8 ($m/z = 274$), P9 ($m/z = 283$), P12 ($m/z = 256$), P13 ($m/z = 225$), P14 ($m/z = 218$), and P10 ($m/z = 282$), respectively [58,59,61,62]. This mainly included dehydration, dealkylation, dihydroxy methylation, and other degradation pathways. P6 was oxidized to P11 ($m/z = 141$) through dehydration and ring opening under the action of·OH [58]. Finally, these small molecules were further oxidized into CO_2 and H_2O to achieve the degradation of TC.

4. Conclusions

In conclusion, a CuCoSi hollow nanosphere catalyst was successfully prepared by a one-step alcohol-thermal method, which showed better activity and stability for activating PMS compared with CoSi. Moreover, the CuCoSi/PMS system showed strong resistance to changes in environmental media, such as pH, inorganic anions, and temperature, indicating the great practical application potential of CuCoSi catalysts. The doped Cu simultaneously promoted the formation of SO_4^-·,·OH and $^1O_2$. Through the micro-mechanism analysis, it was found that Co sites were the unique active sites in the radical pathway. Cu enhanced radical pathway by electron transfer with Co instead of directly participating in the activation of PMS, although CuSi could effectively activate PMS. In the non-radical pathway, the doping with Cu led to the formation of more Ov than in CoSi, which promoted the generation of $^1O_2$. This work has clarified the synergistic effect and mechanism of the bimetal in silicate and provided a theoretical basis for the design and optimization of bimetal catalysts.

CRediT authorship contribution statement

Lu-Lu Long: Conceptualization, Methodology, Formal analysis, Writing – original draft , Writing – review & editing, Project administration. **Lin-Lin Su:** Investigation, Validation, Data analysis, Writing – original draft, Writing – revised, Visualization. **Wei Hu:** Investigation, Sampling. **Shi-Huai Deng:** Supervision, Funding acquisition. **Chao Chen:** Investigation, Formal analysis. **Fei-Shen:** Resources, Writing – review & editing. **Min Xu:** Writing – review & editing. **Gui-xiang Huang**: Writing – review & editing. **Gang Yang:** Resources, Writing – review & editing, Supervision, Funding acquisition.

Declaration of Competing Interest

The authors declare that they have no known competing financial interests or personal relationships that could have appeared to influence the work reported in this paper.

Acknowledgments

Appendix A. Supporting information

Supplementary data associated with this article can be found in the online version at doi:10.1016/j.apcatb.2022.121276.

References

[1] P. Hu, M. Long, Cobalt-catalyzed sulfate radical-based advanced oxidation: A review on heterogeneous catalysts and applications, Appl. Catal. B: Environ. 181 (2016) 103–117.
[2] L. Zhu, J. Ji, J. Liu, S. Mine, M. Matsuoka, J. Zhang, M. Xing, Designing 3D-MoS2 Sponge as Excellent Cocatalysts in Advanced Oxidation Processes for Pollutant Control, Angew. Chem. Int. Ed. Engl. 59 (2020) 13968–13976.
[3] Y. Chen, G. Zhang, H. Liu, J. Qu, Confining free radicals in close vicinity to contaminants enables ultrafast fenton-like processes in the interspacing of MoS2 membranes, Angew. Chem. Int. Ed. Engl. 58 (2019) 8134–8138.
[4] W. Wang, Y. Liu, Y. Yue, H. Wang, G. Cheng, C. Gao, C. Chen, Y. Ai, Z. Chen, X. Wang, The confined interlayer growth of ultrathin two-dimensional fe3o4 nanosheets with enriched oxygen vacancies for peroxymonosulfate activation, ACS Catal. 11 (2021) 11256–11265.
[5] W.D. Oh, Z. Dong, G. Ronn, T.T. Lim, Surface-active bismuth ferrite as superior peroxymonosulfate activator for aqueous sulfamethoxazole removal: Performance, mechanism and quantification of sulfate radical, J. Hazard. Mater. 325 (2017) 71–81.
[6] Y. Gao, Z. Chen, Y. Zhu, T. Li, C. Hu, New INsights Into the Generation of Singlet Oxygen in the Metal-free Peroxymonosulfate Activation Process: Important Role of Electron-deficient Carbon Atoms, Environ. Sci. Technol. 54 (2020) 1232–1241.
[7] G.X. Huang, C.Y. Wang, C.W. Yang, P.C. Guo, H.Q. Yu, Degradation of bisphenol A by peroxymonosulfate catalytically activated with Mn1.8Fe1.2O4 nanospheres: synergism between Mn and Fe, Environ. Sci. Technol. 51 (2017) 12611–12618.
[8] P. Zhang, Y. Yang, X. Duan, Y. Liu, S. Wang, Density functional theory calculations for insight into the heterocatalyst reactivity and mechanism in persulfate-based advanced oxidation reactions, ACS Catal. 11 (2021) 11129–11159.
[9] X. Li, J. Wang, X. Duan, Y. Li, X. Fan, G. Zhang, F. Zhang, W. Peng, Fine-tuning radical/nonradical pathways on graphene by porous engineering and doping strategies, ACS Catal. 11 (2021) 4848–4861.
[10] Y. Wang, H. Sun, H.M. Ang, M.O. Tade, S. Wang, Facile synthesis of hierarchically structured magnetic MnO2/ZnFe2O4 hybrid materials and their performance in heterogeneous activation of peroxymonosulfate, ACS Appl. Mater. Interfaces 6 (2014) 19914–19923.
[11] X. Li, X. Huang, S. Xi, S. Miao, J. Ding, W. Cai, S. Liu, X. Yang, H. Yang, J. Gao, J. Wang, Y. Huang, T. Zhang, B. Liu, Single cobalt atoms anchored on porous N-Doped graphene with dual reaction sites for efficient fenton-like catalysis, J. Am. Chem. Soc. 140 (2018) 12469–12475.
[12] L. Liu, H. Mi, M. Zhang, F. Sun, R. Zhan, H. Zhao, S. He, L. Zhou, Efficient moxifloxacin degradation by CoFe2O4 magnetic nanoparticles activated peroxymonosulfate: kinetics, pathways and mechanisms, Chem. Eng. J. 407 (2021), 127201.
[13] Q. Lian, A. Roy, O. Kizilkaya, D.D. Gang, W. Holmes, M.E. Zappi, X. Zhang, H. Yao, Uniform mesoporous amorphous cobalt-inherent silicon oxide as a highly active heterogeneous catalyst in the activation of peroxymonosulfate for rapid oxidation of 2,4-dichlorophenol: the important role of inherent cobalt in the catalytic mechanism, ACS Appl. Mater. Interfaces 12 (2020) 57190–57206.
[14] Z.Y. Guo, C.X. Li, M. Gao, X. Han, Y.J. Zhang, W.J. Zhang, W.W. Li, Mn-O covalency governs the intrinsic activity of Co-Mn spinel oxides for boosted peroxymonosulfate activation, Angew. Chem. Int. Ed. Engl. 60 (2021) 274–280.
[15] S. Zhan, H. Zhang, X. Mi, Y. Zhao, C. Hu, L. Lyu, Efficient fenton-like process for pollutant removal in electron-rich/poor reaction sites induced by surface oxygen vacancy over cobalt-zinc oxides, Environ. Sci. Technol. 54 (2020) 8333–8343.
[16] L. Wu, B. Li, Y. Li, X. Fan, F. Zhang, G. Zhang, Q. Xia, W. Peng, Preferential Growth of the cobalt (200) facet in Co@N–C for enhanced performance in a fenton-like reaction, ACS Catal. 11 (2021) 5532–5543.
[17] Z. Wu, Y. Wang, Z. Xiong, Z. Ao, S. Pu, G. Yao, B. Lai, Core-shell magnetic Fe3O4@Zn/Co-ZIFs to activate peroxymonosulfate for highly efficient degradation of carbamazepine, Appl. Catal. B: Environ. 277 (2020), 119136.
[18] X. Zhou, C. Luo, M. Luo, Q. Wang, J. Wang, Z. Liao, Z. Chen, Z. Chen, Understanding the synergetic effect from foreign metals in bimetallic oxides for PMS activation: a common strategy to increase the stoichiometric efficiency of oxidants, Chem. Eng. J. 381 (2020), 122587.
[19] R. Guo, Y. Zhu, X. Cheng, J. Li, J.C. Crittenden, Efficient degradation of lomefloxacin by Co-Cu-LDH activating peroxymonosulfate process: optimization, dynamics, degradation pathway and mechanism, J. Hazard. Mater. 399 (2020), 122966.
[20] Q. Yang, H. Choi, S.R. Al-Abed, D.D. Dionysiou, Iron–cobalt mixed oxide nanocatalysts: heterogeneous peroxymonosulfate activation, cobalt leaching, and ferromagnetic properties for environmental applications, Appl. Catal. B: Environ. 88 (2009) 462–469.
[21] C. Wang, J. Zhao, J. Chen, P. Na, Catalytic activation of PS/PMS over Fe-Co bimetallic oxides for phenol oxidation under alkaline conditions, Appl. Surf. Sci. 562 (2021), 150134.
[22] Z. Li, F. Wang, Y. Zhang, Y. Lai, Q. Fang, Y. Duan, Activation of peroxymonosulfate by CuFe2O4-CoFe2O4 composite catalyst for efficient bisphenol a degradation: synthesis, catalytic mechanism and products toxicity assessment, Chem. Eng. J. 423 (2021), 130093.
[23] Z.-S. Zhu, X.-J. Yu, J. Qu, Y.-Q. Jing, Y. Abdelkrim, Z.-Z. Yu, Preforming abundant surface cobalt hydroxyl groups on low crystalline flowerlike Co3(Si2O5)2(OH)2 for enhancing catalytic degradation performances with a critical nonradical reaction, Appl. Catal. B: Environ. 261 (2020), 118238.
[24] S.M. Hao, M.Y. Yu, Y.J. Zhang, Y. Abdelkrim, J. Qu, Hierarchical mesoporous cobalt silicate architectures as high-performance sulfate-radical-based advanced oxidization catalysts, J. Colloid Interface Sci. 545 (2019) 128–137.
[25] J.F.G. Kresse, 1996. Efficiency of ab-initio total energy calculations for metals and semiconductors using a plane-wave basis set computational materials science, (1996) 15–50.
[26] J.F.G. Kresse, Efficient iterative schemes for ab initio total-energy calculations using a plane-wave basis set, Physical Review B, 54 (J. Furthmuller).
[27] K.B. John, P. Perdew, Matthias ernzerhof, generalized gradient approximation made simple, Phys. Rev. Lett. 77 (1996).

[28] D.J.G. Kresse, From ultrasoft pseudopotentials to the projector augmented-wave method, Phys. Rev. B 59 (1998).

[29] P.E. Blöchl, Projector augmented-wave method, Phys. Rev. B 50 (1994) 17953–17979.

[30] S. Grimme, J. Antony, S. Ehrlich, H. Krieg, A consistent and accurate ab initio parametrization of density functional dispersion correction (DFT-D) for the 94 elements H-Pu, J. Chem. Phys. 132 (2010) 154104.

[31] G. Zhan, H.C. Zeng, Topological transformations of core-shell precursors to hierarchically hollow assemblages of copper silicate nanotubes, ACS Appl. Mater. Interfaces 9 (2017) 37210–37218.

[32] M. Srinivas, P. Srinivasu, S.K. Bhargava, M.L. Kantam, Direct synthesis of two-dimensional mesoporous copper silicate as an efficient catalyst for synthesis of propargylamines, Catal. Today 208 (2013) 66–71.

[33] Y. Pan, Y. Lin, Y. Liu, C. Liu, A novel CoP/MoS2-CNTs hybrid catalyst with Pt-like activity for hydrogen evolution, Catal. Sci. Technol. 6 (2016) 1611–1615.

[34] J. Jagiello, A. Chojnacka, S.E.M. Pourhosseini, Z. Wang, F. Beguin, A dual shape pore model to analyze the gas adsorption data of hierarchical micro-mesoporous carbons, Carbon 178 (2021) 113–124.

[35] C.-X. Li, C.-B. Chen, J.-Y. Lu, S. Cui, J. Li, H.-Q. Liu, W.-W. Li, F. Zhang, Metal organic framework-derived CoMn$_2$O$_4$ catalyst for heterogeneous activation of peroxymonosulfate and sulfanilamide degradation, Chem. Eng. J. 337 (2018) 101–109.

[36] P. Shao, J. Tian, X. Duan, Y. Yang, W. Shi, X. Luo, F. Cui, S. Luo, S. Wang, Cobalt silicate hydroxide nanosheets in hierarchical hollow architecture with maximized cobalt active site for catalytic oxidation, Chem. Eng. J. 359 (2019) 79–87.

[37] A.-Y. Zhang, Y.-Y. He, Y.-P. Chen, J.-W. Feng, N.-H. Huang, F. Lian, Degradation of organic pollutants by Co$_3$O$_4$-mediated peroxymonosulfate oxidation: roles of high-energy {0 0 1}-exposed TiO$_2$ support, Chem. Eng. J. 334 (2018) 1430–1439.

[38] Z.-J. Xiao, X.-C. Feng, H.-T. Shi, B.-Q. Zhou, W.-Q. Wang, N.-Q. Ren, Why the cooperation of radical and non-radical pathways in PMS system leads to a higher efficiency than a single pathway in tetracycline degradation, J. Hazard. Mater. 424 (2022), 127247.

[39] Y. Zhou, Y. Gao, J. Jiang, Y.-M. Shen, S.-Y. Pang, Z. Wang, J. Duan, Q. Guo, C. Guan, J. Ma, Transformation of tetracycline antibiotics during water treatment with unactivated peroxymonosulfate, Chem. Eng. J. 379 (2020), 122378.

[40] S. Zhang, X. Ren, X. Zhou, H. Gao, X. Wang, J. Huang, X. Xu, Hierarchical multi-active component yolk-shell nanoreactors as highly active peroxymonosulfate activator for ciprofloxacin degradation, J. Colloid Interface Sci. 605 (2022) 766–778.

[41] X. Zhang, R. Zhao, N. Zhang, Y. Su, Z. Liu, R. Gao, C. Du, Insight to unprecedented catalytic activity of double-nitrogen defective metal-free catalyst: Key role of coal gangue, Appl. Catal. B: Environ. 263 (2020), 127997.

[42] N. Li, R. Li, X. Duan, B. Yan, W. Liu, Z. Cheng, G. Chen, L. Hou, S. Wang, Correlation of active sites to generated reactive species and degradation routes of organics in peroxymonosulfate activation by Co-loaded carbon, Environ. Sci. Technol. 55 (2021) 16163–16174.

[43] X. Long, C. Feng, D. Ding, N. Chen, S. Yang, H. Chen, X. Wang, R. Chen, Oxygen vacancies-enriched CoFe$_2$O$_4$ for peroxymonosulfate activation: The reactivity between radical-nonradical coupling way and bisphenol A, J. Hazard. Mater. 418 (2021) 126357.

[44] J. Xie, Z. Liao, M. Zhang, L. Ni, J. Qi, C. Wang, X. Sun, L. Wang, S. Wang, J. Li, Sequential ultrafiltration-catalysis membrane for excellent removal of multiple pollutants in water, Environ. Sci. Technol. 55 (2021) 2652–2661.

[45] G. Lan, K. Ni, S.S. Veroneau, T. Luo, E. You, W. Lin, Nanoscale metal-organic framework hierarchically combines high-Z components for multifarious radio-enhancement, J. Am. Chem. Soc. 141 (2019) 6859–6863.

[46] S. Yang, X. Duan, J. Liu, P. Wu, C. Li, X. Dong, N. Zhu, D.D. Dionysiou, Efficient peroxymonosulfate activation and bisphenol A degradation derived from mineral-carbon materials: key role of double mineral-templates, Appl. Catal. B: Environ. 267 (2020), 118701.

[47] X. Mi, P. Wang, S. Xu, L. Su, H. Zhong, H. Wang, Y. Li, S. Zhan, Almost 100% peroxymonosulfate conversion to singlet oxygen on single-atom CoN2+2 sites, Angew. Chem. Int Ed. Engl. 60 (2021) 4588–4593.

[48] L. Luo, Y. Wang, M. Zhu, X. Cheng, X. Zhang, X. Meng, X. Huang, H. Hao, Co–Cu–Al layered double oxides as heterogeneous catalyst for enhanced degradation of organic pollutants in wastewater by activating peroxymonosulfate: performance and synergistic effect, Ind. Eng. Chem. Res. 695 (2019), 133596.

[49] Y. Li, Z. Fan, J. Shi, Z. Liu, J. Zhou, W. Shangguan, Modified manganese oxide octahedral molecular sieves M′-OMS-2 (M′ = Co,Ce,Cu) as catalysts in post plasma-catalysis for acetaldehyde degradation, Catal. Today 256 (2015) 178–185.

[50] X. Yao, Y. Li, Z. Fan, Z. Zhang, M. Chen, W. Shangguan, Plasma catalytic removal of hexanal over Co–Mn solid solution: effect of preparation method and synergistic reaction of ozone, Ind. Eng. Chem. Res. 57 (2018) 4214–4224.

[51] X. Yao, M. Gao, Z. Wei, M. Chen, W. Shangguan, Removal of hexanal in cooking fume by combination of storage and plasma-catalytic oxidation on alkali-modified Co-Mn solid solution, Chemosphere 220 (2019) 738–747.

[52] L. Wu, Z. Sun, Y. Zhen, S. Zhu, C. Yang, J. Lu, Y. Tian, D. Zhong, J. Ma, Oxygen vacancy-induced nonradical degradation of organics: critical trigger of oxygen (O2) in the Fe-Co LDH/peroxymonosulfate system, Environ. Sci. Technol. 55 (2021) 15400–15411.

[53] X. Duan, Z. Ao, L. Zhou, H. Sun, G. Wang, S. Wang, Occurrence of radical and nonradical pathways from carbocatalysts for aqueous and nonaqueous catalytic oxidation, Appl. Catal. B: Environ. 188 (2016) 98–105.

[54] H. Chen, Y. Xu, K. Zhu, H. Zhang, Understanding oxygen-deficient La2CuO4-δperovskite activated peroxymonosulfate for bisphenol A degradation: the role of localized electron within oxygen vacancy, Appl. Catal. B: Environ. 284 (2021), 119732.

[55] Y. Ren, L. Lin, J. Ma, J. Yang, J. Feng, Z. Fan, Sulfate radicals induced from peroxymonosulfate by magnetic ferrospinel MFe2O4 (M = Co, Cu, Mn, and Zn) as heterogeneous catalysts in the water, Appl. Catal. B: Environ. 165 (2015) 572–578.

[56] D.G. Van Campen, L.E. Klebanoff, Spin-resolved and high-energy-resolution XPS studies of the 3sand 2slevels of metallic cobalt, Phys. Rev. B 49 (1994) 2040–2046.

[57] J. Wang, S. Wang, Activation of persulfate (PS) and peroxymonosulfate (PMS) and application for the degradation of emerging contaminants, Chem. Eng. J. 334 (2018) 1502–1517.

[58] Q. Hu, J. Cao, Z. Yang, W. Xiong, Z. Xu, P. Song, M. Jia, Y. Zhang, H. Peng, A. Wu, Fabrication of Fe-doped cobalt zeolitic imidazolate framework derived from Co (OH)$_2$ for degradation of tetracycline via peroxymonosulfate activation, Sep. Purif. Technol. 259 (2021) 118059.

[59] X. Li, T. Hou, L. Yan, L. Shan, X. Meng, Y. Zhao, Efficient degradation of tetracycline by CoFeLa-layered double hydroxides catalyzed peroxymonosulfate: Synergistic effect of radical and nonradical pathways, J. Hazard. Mater. 398 (2020) 122884.

[60] M. Shen, Z. Huang, X. Luo, Y. Ma, C. Chen, X. Chen, L. Cui, Activation of persulfate for tetracycline degradation using the catalyst regenerated from Fenton sludge containing heavy metal: synergistic effect of Cu for catalysis, Chem. Eng. J. 396 (2020) 125238.

[61] Y. Wang, J. Cao, Z. Yang, W. Xiong, Z. Xu, P. Song, M. Jia, S. Sun, Y. Zhang, W. Li, Fabricating iron-cobalt layered double hydroxide derived from metal-organic framework for the activation of peroxymonosulfate towards tetracycline degradation, J. Solid State Chem. 294 (2021), 121857.

[62] F. Liu, J. Cao, Z. Yang, W. Xiong, Z. Xu, P. Song, M. Jia, S. Sun, Y. Zhang, X. Zhong, Heterogeneous activation of peroxymonosulfate by cobalt-doped MIL-53(Al) for efficient tetracycline degradation in water: coexistence of radical and non-radical reactions, J. Colloid Interface Sci. 581 (2021) 195–204.